Broadband Acoustic Hyperbolic Metamaterial

Chen Shen, Yangbo Xie, Ni Sui, Wenqi Wang, Steven A. Cummer, and Yun Jing

Phys. Rev. Lett. **115**, 254301 — Published 16 December 2015

DOI: 10.1103/PhysRevLett.115.254301

Broadband Acoustic Hyperbolic Metamaterial

Chen Shen[1], Yangbo Xie[2], Ni Sui[1], Wenqi Wang[2], Steven A. Cummer[2] and Yun Jing[1,†]

[1]Department of Mechanical and Aerospace Engineering, North Carolina State University, Raleigh, North Carolina 27695, USA

[2]Department of Electrical and Computer Engineering, Duke University, Durham, North Carolina 27708, USA

[†]Corresponding author
yjing2@ncsu.edu

PACS numbers: 43.20.+g, 43.58.+z, 46.40.Cd

Abstract

In this Letter, we report on the design and experimental characterization of a broadband acoustic hyperbolic metamaterial. The proposed metamaterial consists of multiple arrays of clamped thin plates facing the y-direction and is shown to yield opposite signs of effective density in x- and y-directions below a certain cutoff frequency, therefore yielding a hyperbolic dispersion. Partial focusing and subwavelength imaging are experimentally demonstrated at frequencies between 1.0 kHz and 2.5 kHz. The proposed metamaterial could open up new possibilities for acoustic wave manipulation and may find usage in medical imaging and non-destructive testing.

Acoustic metamaterials (AMMs) are engineered materials, made from subwavelength structures, that exhibit useful or unusual constitutive properties. There has been intense research interest in AMMs since its first realization in 2000 by Liu *et al* [1]. A number of functionalities and applications have been proposed and achieved using AMMs [2–9]. Hyperbolic metamaterials are one of the most important types of metamaterials due to their extreme anisotropy and numerous possible applications, including negative refraction, backward waves, spatial filtering, and subwavelength imaging [10–12]. Acoustic hyperbolic metamaterials (AHMMs) are AMMs that have extremely anisotropic densities. In two-dimensional (2D) scenarios, the density is positive in one direction and negative in the orthogonal direction. For materials with anisotropic densities, the general dispersion relation is given by $\frac{k_x^2}{\rho_x}+\frac{k_y^2}{\rho_y}=\frac{\omega^2}{B}$, where k and ω are the wave number and angular frequency, respectively, B is the bulk modulus of the entire medium. For media with positive, anisotropic densities, the equifrequency contour (EFC) is an ellipse, whereas it is a hyperbola for AHMMs. Although the importance of AHMMs as a tool for achieving full control of acoustic waves is substantial, the realization of a broadband and truly hyperbolic AMM has not been reported so far. A broadband hyperlens has been demonstrated using brass fins [13]. The capability of subwavelength imaging, however, stems from extreme contrast of density and

this hyperlens in fact does not bear a hyperbolic dispersion. It has been shown theoretically and experimentally that periodically perforated plates can exhibit hyperbolic-like dispersion for airborne sound [14,15]. Negative refraction and energy funneling associated with this structure were demonstrated experimentally within a narrow band around 40 kHz. This design yields a flat band profile in EFC and therefore could not demonstrate acoustic partial focusing, which is an important application of AHMMs.

In this work, we show the realization of a broadband AHMM utilizing plate-(membrane-) type AMMs [16–21]. The proposed structure exhibits truly hyperbolic dispersion, as demonstrated by its ability of partial focusing and subwavelength imaging over a broadband frequency. The design of the AHMM is illustrated in Fig. 1. The rigid frames are made of aluminum and the thin plates are made of hard paper. There are 13 frames and each contains 14 plate unit cells. The boundaries of the plates are fixed securely on the aluminum frames to achieve the clamped boundary condition. No tension is applied on the plates. Two acrylic panels cover the top and bottom of the sample to ensure two-dimensional wave propagation.

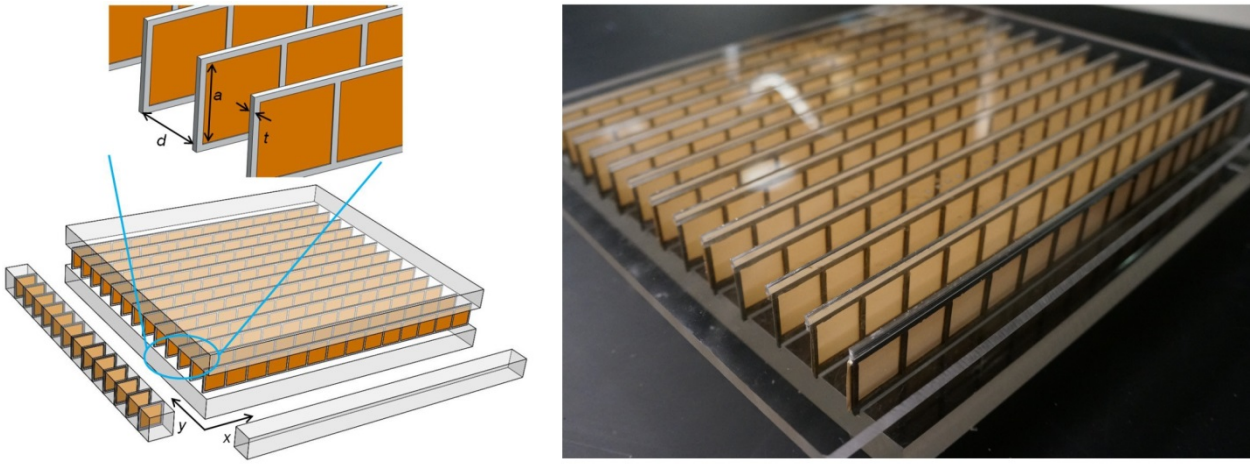

Figure 1. (Color online) Snapshots of the AHMM. (a) Physical structure of the AHMM. Each two frames have a separation distance of $d = 2$ cm and the thickness of the frame is $t = 0.16$ cm. The frames in the y-direction therefore have a periodicity of $D = d + t = 2.16$ cm. The width of the square plate is $a = 2$ cm. To study the effective acoustic properties, the 2D AHMM can be decoupled into two waveguides in each direction: one contains periodically arranged plates (y-direction) and the other does not (x-direction). (b) Photo of the fabricated AHMM sample. The size of the sample is 30.2 cm by 27 cm.

To theoretically characterize the proposed AHMM, we use one-dimensional (1D) analysis since wave propagation in x- and y-directions can be decoupled in this type of structure [17,19]. In other words, the effective acoustic property in x- and y-directions can be estimated by using 1D waveguide structures as shown in Fig.1. The bulk modulus of the structure is assumed to be the same with air, since the thin plates have a negligible effect on the effective bulk modulus as demonstrated in [17,19]. Because there are no plates arranged in the x-direction, the effective

density can be considered as that of air and is frequency-independent ($\rho_x = 1.2\ \mathrm{kg/m^3}$). In the y-direction, a lumped model can be utilized to predict the frequency-dependent effective density [19], which is written as $\rho_y = \frac{Z_{am}}{j\omega} \cdot \frac{1}{DA}$, where Z_{am} is the acoustic impedance of the plate, $A = a^2$ is the cross-sectional area of the waveguide. Since there is no closed form solution of Z_{am} for a square plate, the acoustic impedance is calculated by the finite element method and is $Z_{am} = \frac{Z_m}{A^2} = \frac{\iint \Delta p A}{j\omega \xi A^2}$ [19], where Z_m is the mechanical impedance of the plate, Δp is the pressure difference across the plate, and ξ denotes the average transverse displacement of the plate. The plate has a density 591 $\mathrm{kg/m^3}$ and a thickness 0.3 mm. The flexural rigidity of the plate D' is estimated to be around 0.0066 $\mathrm{Pa \cdot m^4}$, which is retrieved by measuring the first resonance frequency of a single clamped square plate. The Young's modulus and Poisson's ratio are estimated to be 2.61 GPa and 0.33, respectively [22]. The resonance frequency of a clamped square plate is given by $f_0 = \frac{5.58}{A}\sqrt{\frac{D'}{\rho h}}$ [24]. For the designed plate, the first resonance frequency (or cutoff frequency) is about 2.69 kHz. Figures 2(a) and (b) show the predicted effective density and the corresponding EFC at relevant frequencies. ρ_y is close to zero around the cutoff frequency and negative below the cutoff frequency [16,19,25]. Since ρ_x is always positive, the dispersion curve theoretically is a hyperbola over a broadband frequency. Two sets of results for the EFC are shown and are in good agreement. One is calculated using the effective density from the lumped model and the other one is from numerical simulations of the real structure without assuming homogenization. For the numerical results, the band structure of a unit cell is first studied [22], and the EFC is retrieved from the band structure.

When the acoustic waves (red solid line in Fig. 2(b)) propagate from free space (black dotted curve) into the hyperbolic medium (purple solid curve) at a certain angle, the refractive angle is negative, since the group velocity v_g must lie normal to the EFC. As a result, partial acoustic focusing can be achieved [12]. By combining the dispersion relation of free space and the hyperbolic medium, the refraction angle of an incident wave vector k_i with vertical component k_y can be calculated as:

$$\theta_r = \pm \tan^{-1} \frac{\rho_x}{\rho_y} \left(k_y \Big/ \left(\rho_x \left(\frac{\omega^2}{B} - \frac{k_y^2}{\rho_y} \right) \right)^{\frac{1}{2}} \right). \tag{1}$$

The sign should be determined so that the refraction angle has the opposite sign with k_y. As seen from Fig. 2(a), at frequencies sufficiently below the cutoff frequency, ρ_y becomes deep negative.

According to Eq. (1), the resulting refraction angle would approach zero, indicating that the focusing effect cannot be observed for an AHMM with a finite size. Since the fabricated AHMM is about 1-2 wavelengths at frequencies of interest, partial focusing effect can be best observed when the absolute value of ρ_y is comparable to the background medium, which occurs at frequencies relatively close to the cutoff frequency.

By rearranging terms in the dispersion equation, one can see that $k_x^2 = \rho_x \left(\frac{\omega^2}{B} - \frac{k_y^2}{\rho_y} \right)$, which indicates that in the absence of losses, there does not exist a value for k_y so that $k_x^2 < 0$ since ρ_y is negative and ρ_x is positive. Consequently, all waves inside the AHMM are in propagating mode and no evanescent solutions are allowed. In other words, at an arbitrary incident angle, the evanescent wave reaching the surface of the AHMM can excite the propagating mode. Furthermore, the EFC becomes flat at frequencies sufficiently below the cutoff frequency, as the absolute value of the effective density in the y-direction is large (Fig. 2(a)). It can be predicted from Fig. 2(b) that at low frequencies, the refracted acoustic waves would be collimated along the x-direction and funneled through the AHMM. Altogether, subwavelength information can be transferred to the opposite side of the AHMM and subwavelength imaging is possible.

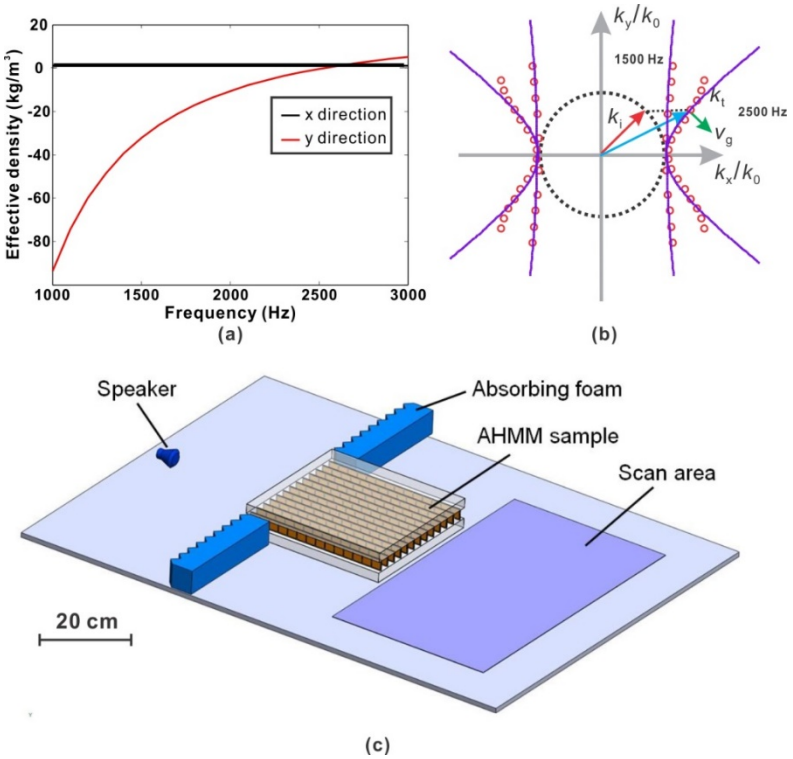

Figure 2. (Color online) Material properties of the AHMM and schematic of the experimental setup. (a) Predicted effective density along x- and y-directions. (b) Calculated EFC at two selected frequencies which are both below the cutoff frequency. The dispersion curves are clearly hyperbolic and the EFCs become flat at low frequencies. Solid line: lumped model. Circle

mark: retrieved from numerical simulations. (c) A loudspeaker mimicking a point source is placed 170 mm away from the front face of the sample. Sound absorptive materials are placed on the edges of the 2D waveguide and two sides of the AHMM sample to minimize the reflection and sound field interference behind the AHMM, respectively.

Both numerical simulations and experiments are conducted to validate the proposed AHMM for partial focusing first. For numerical simulations, the commercial package COMSOL MULTIPHYSICS 5.1 is adopted. The setup for the experiment is depicted in Fig. 2(c) where a loudspeaker mimicking a point source is placed 170 mm away from the front face of the sample. The measurement is conducted inside a 2D waveguide. The loudspeaker transmits pulsed signals at various center frequencies with a bandwidth of 1 kHz and the pressure fields are measured behind the sample. The field mapping measurements are performed using a scanning microphone having a diameter of 10 mm. The scan area is 520 mm×800 mm and the scanning step size is 20 mm. At each position the acoustic pressures are averaged over five measurements. After scanning, the frequency-domain acoustic fields are obtained via the Fourier transform.

Figure 3(a) shows the simulated and measured acoustic pressure fields at 2440 Hz for both cases where the AHMM is present and absent. The acoustic energy is focused on the back of the AHMM and diverges behind the AHMM, as shown by both simulations and experiments. The measurement agrees well with the simulation in terms of the pressure pattern. The pressure magnitude distributions on the exiting surface of the AHMM are also examined. Two types of simulations are performed. One uses the real structure of the AHMM and the other one uses effective medium with properties given by Fig. 2(a). Several factors could contribute to the small discrepancy between the measurement and simulation results: inherent microphone measurement errors (finite size effect, noise, directivity, etc.); some sound could still go through the absorbing foams and interfere with the sound field in the scanning area; the simulation assumes an ideal situation in which the frames are infinitely small and perfectly rigid. Although only partial focusing is achieved, the AHMM may still be favorable over an isotropic negative index metamaterial in terms of energy focusing as it is less sensitive to material loss [26]. When the frequency is above the cutoff, ρ_y becomes positive and the EFC of the AMM changes from a hyperbolic one to an elliptical one. The results at such a frequency can be found in the Supplementary Material [22]. To further validate the effective medium model, which are the theoretical bases for designing the proposed AHMM, quantitative analysis is conducted for negative refraction in a long AHMM slab and the results can be found in the Supplementary Material [22].

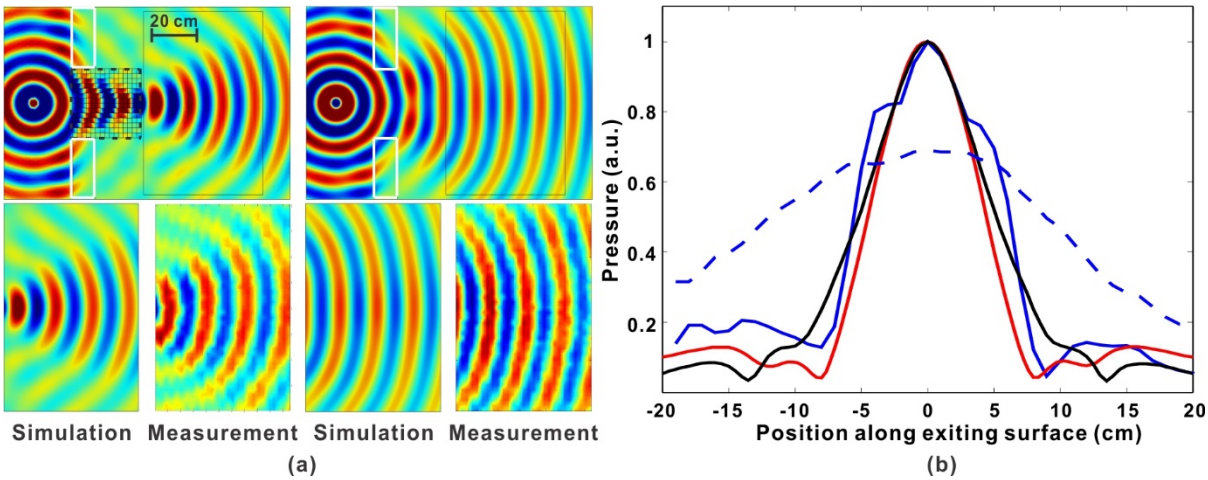

Figure 3. (Color online) Simulated and measured acoustic field showing partial focusing. (a) Acoustic pressure field at 2440 Hz. Top two figures show the simulation results for the entire domain. Left one is with AHMM and right one is without AHMM. Bottom figures compare the simulation and measurement in the scanning area. The solid white box, dashed black box and solid black box denote absorbing foam, AHMM and scan area, respectively. (b) Normalized pressure magnitude distribution on the exiting surface of the AHMM. A focused profile can be clearly observed. Blue (solid): measurement with AHMM; blue (dashed): measurement without AHMM; red: simulation (real structure); black: simulation (effective medium).

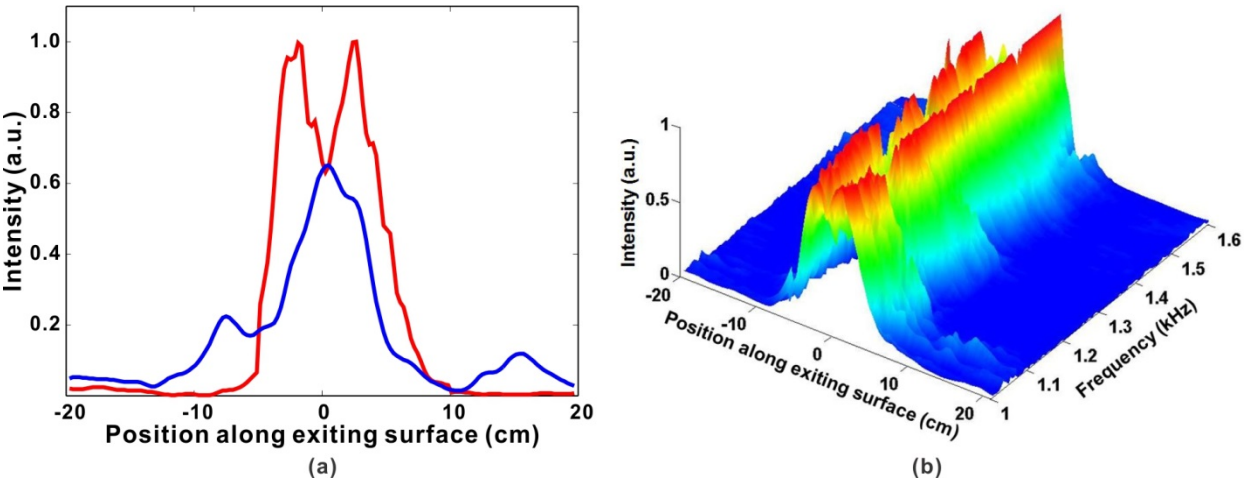

Figure 4 Measured acoustic fields demonstrating subwavelength imaging. (a) Imaging performance of the AHMM at 1.1 kHz. At this frequency, the resolved resolution is about 1/4.7 of the wavelength. The normalized acoustic intensity distribution along the exiting surface of the AHMM clearly shows two peaks, while the control case (without AHMM) shows a single peak. (b) The broadband performance of subwavelength imaging of the AHMM. Two peaks are resolved within a broad frequency band (1 kHz-1.6 kHz).

The AHMM is also capable of subwavelength imaging as abovementioned. To demonstrate subwavelength imaging, a perforated panel with two square holes is placed in front of the AHMM, creating two in-phase sources separated by approximately 66 mm. The acoustic field is measured on the exiting surface of the AHMM at frequencies between 1 kHz and 1.6 kHz. The separation distance therefore corresponds to $\lambda/5.2$-$\lambda/3.2$. The thickness of the AHMM corresponds to 0.9λ-1.4λ. Experimental results are shown in Fig. 4. At 1.1 kHz, two peaks are clearly resolved when the AHMM is present (Fig. 4(a)). When the AHMM is absent (control case), the waves radiated by the two sources merge and the resulting acoustic pressure field shows only one pronounced peak. The total sound intensity also appears to be greater when the AHMM is present compared to the control case. This is possibly because the evanescent wave components, containing subwavelength information, are converted into the propagating components and the energy is transferred to the image plane through the AHMM, while in the control case the evanescent wave components decay very quickly and cannot reach the image plane. The enhanced transmission of evanescent waves is shown in the Supplementary Material [22]. Figure 4b demonstrates the broadband performance of the AHMM. Two peaks can be observed for all frequencies within the frequency range tested.

To conclude, we have designed, fabricated, and tested a broadband AHMM based on plate-type AMMs. Partial focusing and subwavelength imaging are experimentally demonstrated within a broad frequency band, which verifies that such an AMM yields a truly hyperbolic dispersion. The AHMM proposed in this study can be scaled down to operate at much higher frequencies. However, it should be borne in mind that the required high-resolution fabrication can pose a challenge. For example, the unit cell length could be in the 100 micron range for an operating frequency around 1 MHz in water. The proposed AHMM may find usage in angular filtering [27], medical imaging and non-destructive testing. The proposed design can be readily extended to achieve three-dimensional AHMMs. We expect that the results of this paper will provide a new design methodology for the realization of AMMs requiring anisotropic densities.

Acknowledgements

This work was partially supported by the Multidisciplinary University Research Initiative grant from the Office of Naval Research (N00014-13-1-0631).

References

[1] Z. Liu, X. Zhang, Y. Mao, Y. Zhu, and Z. Yang, Science **289**, 1734 (2000).

[2] Y. Ding, Z. Liu, C. Qiu, and J. Shi, Phys. Rev. Lett. **99**, 093904 (2007).

[3] J. Zhu, J. Christensen, J. Jung, L. Martin-Moreno, X. Yin, L. Fok, X. Zhang, and F. J. Garcia-Vidal, Nat. Phys. **7**, 52 (2011).

[4] X. Zhou and G. Hu, Appl. Phys. Lett. **98**, 263510 (2011).

[5] X. Zhu, B. Liang, W. Kan, X. Zou, and J. Cheng, Phys. Rev. Lett. **106**, 014301 (2011).

[6] S. Zhang, C. Xia, and N. Fang, Phys. Rev. Lett. **106**, 024301 (2011).

[7] Y. Xie, B.-I. Popa, L. Zigoneanu, and S. A. Cummer, Phys. Rev. Lett. **110**, 175501 (2013).

[8] G. Ma, M. Yang, S. Xiao, Z. Yang, and P. Sheng, Nat. Mater. **13**, 873 (2014).

[9] L. Zigoneanu, B.-I. Popa, and S. A Cummer, Nat. Mater. **13**, 352 (2014).

[10] X. Ao and C. T. Chan, Phys. Rev. E **77**, 025601 (2008).

[11] D. Lu and Z. Liu, Nat. Commun. **3**, 1205 (2012).

[12] A. Poddubny, I. Iorsh, P. Belov, and Y. Kivshar, Nat. Photonics **7**, 948 (2013).

[13] J. Li, L. Fok, X. Yin, G. Bartal, and X. Zhang, Nat. Mater. **8**, 931 (2009).

[14] J. Christensen and F. García de Abajo, Phys. Rev. Lett. **108**, 124301 (2012).

[15] V. M. García-Chocano, J. Christensen, and J. Sánchez-Dehesa, Phys. Rev. Lett. **112**, 144301 (2014).

[16] S. H. Lee, C. M. Park, Y. M. Seo, Z. G. Wang, and C. K. Kim, Phys. Lett. A **373**, 4464 (2009).

[17] C. M. Park, J. J. Park, S. H. Lee, Y. M. Seo, C. K. Kim, and S. H. Lee, Phys. Rev. Lett. **107**, 194301 (2011).

[18] R. Fleury and A. Alù, Phys. Rev. Lett. **111**, 055501 (2013).

[19] C. Shen, J. Xu, N. X. Fang, and Y. Jing, Phys. Rev. X **4**, 041033 (2014).

[20] N. Sui, X. Yan, T.-Y. Huang, J. Xu, F.-G. Yuan, and Y. Jing, Appl. Phys. Lett. **106**, 171905 (2015).

[21] X. Xu, P. Li, X. Zhou, and G. Hu, EPL (Europhysics Lett). **109**, 28001 (2015).

[22] See Supplemental Material [url], which includes Ref. [23], for the determination of flexural rigidity of the plates, band structure of the AHMM unit cell, simulation and measurement above the cutoff frequency of the plate, validation of broadband negative refraction and enhanced transmission of evanescent waves.

[23] F. Bongard, H. Lissek, and J. R. Mosig, Phys. Rev. B **82**, 094306 (2010).

[24] A. W. Leissa, Vibration of plates, NASA SP-160 (1969).

[25] Y. Jing, J. Xu, and N. X. Fang, Phys. Lett. A **376**, 2834 (2012).

[26] D. Smith and D. Schurig, Phys. Rev. Lett. **90**, 077405 (2003).

[27] D. Schurig and D. R. Smith, Appl. Phys. Lett. **82**, 2215 (2003).